




Effects of rotation on a phononic crystal operated in whispering gallery modesFei Ge , Liye Zhao ,* Jiawen Xu, and Xukai Ding*Key Laboratory of Micro-Inertial Instrument and Advanced Navigation Technology, Ministry of Education, School of Instrument Science and Engineering, Southeast University, China* (Received 25 September 2023; revised 12 December 2023; accepted 3 January 2024; published 18 January 2024)

In this paper, the effects of rotation on a phononic crystal (PnC) operated in whispering-gallery modes (WGMs) are investigated for the first time. According to the results of a finite element method, the vibration pattern of the WGMs under the action of rotation will undergo a linear precession with the integral of rotation, which agrees with the theoretical models. In addition, the precession of WGMs will linearly induce a phase difference between the transmissive waves with a fixed phase gain. The difference displacement is utilized to characterize the effects of rotation on the transmissive wave, showing periodicity, linearity, and directionality as theoretical predictions. These findings offer a rate-integrating scheme to sense rotation and have promising applications, especially in high-performance SAW gyroscopes.

DOI: [10.1103/PhysRevB.109.024107](https://doi.org/10.1103/PhysRevB.109.024107)**I. INTRODUCTION**

Due to their distinguished capability of artificially manipulating acoustic/elastic waves, phononic crystals (PnCs) possess numerous promising applications such as sensing [1–4], waveguides [5–7], filters [8,9], energy harvesting [10,11], vibration reduction [12,13], and acousto-optic coupling [14,15]. Especially, the solid media-based PnCs that control elastic waves like bulk waves [16], surface acoustic waves (SAW, Rayleigh waves [17,18], Lamb waves [19–22], and Love waves [23]) are receiving increasing interest for the potential in high-performance MEMS devices. Among these solid media-based PnCs, one prominent structure is periodic hollow pillars on substrate with plentiful related works reported. Jin *et al.* [24–26] demonstrated the existence of whispering gallery modes (WGMs) in the hollow-pillar PnCs, and numerically studied their multiplexing properties. Experimentally, Yuan *et al.* [27] reported the guiding achievements and emphasized the role played by WGMs of the hollow pillars. Subsequently, Muhammad *et al.* [28] studied the interaction of WGMs with Rayleigh waves, and they investigated the wave multiplexing phenomena for all types of waveguides. Unlike the solid pillars that are common to adopt, hollow pillars feature high- Q localized WGMs and interaction with SAWs both of Lamb and Rayleigh waves, hence allowing for high-performance guiding, filtering and sensing.

In fact, the WGMs in PnCs are very similar to the working modes of hemispherical resonance gyroscopes (HRGs) [29–31], which are of the highest accuracy and the best overall performance among the Coriolis vibration gyroscopes. Therefore it is conceivable that the WGMs in PnCs may be affected by rotation, and in turn, the PnCs operated in WGMs may sense the rotation. And this rotation sensing based on SAWs features extremely impact resistant (even $2e^5g$) [32,33],

which is particularly meaningful in extreme working environments (e.g., rocket launch, ammunition penetration, oil field drilling). However, current efforts on PnCs operated in WGMs are all focused on functional devices such as waveguides and filters, and have not addressed the role of rotation.

In this paper, we investigate the effects of rotation on the PnC operated in WGMs, especially on the point-defect PnC. Both the frequency-domain and time-domain results are calculated with the finite element method (FEM, COMSOL MULTIPHYSICS). The contents are arranged into five sections. In Sec. II, the properties of the WGMs in a unit cell are studied. In Sec. III, the effects of rotation on the WGMs and the transmissive waves of a point-defect PnC are demonstrated. In Sec. IV, we further discuss the application of findings on SAW gyroscopes. Finally, we conclude this paper in Sec. V.

II. UNIT CELLS UNDER ROTATION

A hollow pillar with square plate is considered as the unit cell of the PnCs. The hollow pillar makes the localized modes of WGMs access, and the extra layer between hollow pillar and plate can significantly enhance the quality factor of WGMs [24]. Isotropic single-crystal silicon is chosen for both the substrate plate and the pillars, whose mass density is 2329 kg/m^3 , Young's modulus is 170 GPa and poisson ratio is 0.28 . And the structure parameters are decided as plate thickness $e = 0.2a$, inner height $hi = 0.45a$, outer height $ho = 0.65a$, outer radius $ro = 0.3a$, and thickness of hollow wall $b = 0.05a$ after optimization to a high- Q factor, where a is the lattice constant. The hollow-pillar unit cell constructed in Structural mechanics module of COMSOL, shown in Fig. 1, are employed to calculate the dispersion curves or the band structures. Periodic boundary conditions and rotation boundary conditions are applied, and the frequency is normalized by a function, $\Omega_{\text{Norm}} = \omega a / (2\pi v_t)$, where $v_t = 5844 \text{ m/s}$.

The cases in this paper can be treated as the linear problems of small elastic deformations. In fact, this treatment is widely

*liyehao@seu.edu.cn

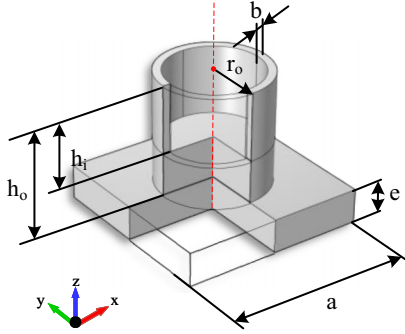


FIG. 1. Unit cell of the PnCs composed with a thin plate and a hollow pillar. Both the plate and pillar are isotropic single-crystal silicon. $e = 0.2a$, $h_i = 0.45a$, $h_o = 0.65a$, $r_o = 0.3a$, and $b = 0.05a$.

employed in studying the PnCs based on elastic materials [24,34,35] and also shows agreement with experimental results [27,36,37]. The usual (in an inertial frame) small elastic deformation problems are solved in COMSOL by combining the constitutive equation, the kinematic equilibrium equation, and strain-compatibility equation [38]. The three equations are expressed successively as

$$\begin{aligned} \sigma &= C_e \varepsilon, \\ \rho \frac{\partial^2 \mathbf{u}}{\partial t^2} &= \nabla \sigma + \mathbf{F}_V, \\ \varepsilon &= [(\nabla \mathbf{u}^T + \nabla \mathbf{u})]/2, \end{aligned} \quad (1)$$

where σ , ε , and \mathbf{u} are three variables to be determined, representing stress, strain, and displacement, respectively. C_e is the elastic matrix of material, and \mathbf{F}_V is the volume force per unit volume. When the rotation boundary condition is applied, the cases are in a rotating frame (a noninertial frame), where Newton's laws may fail and the "fictitious" forces such as Coriolis and centrifugal forces need to be considered. Therefore the kinematic equilibrium equation under rotation is modified as

$$\rho \left(\frac{\partial^2 \mathbf{u}_r}{\partial t^2} + \mathbf{a}_{\text{cor}} + \mathbf{a}_{\text{cen}} \right) = \nabla \sigma + \mathbf{F}_V, \quad (2)$$

where \mathbf{u}_r is the displacement in the rotating frame. $\mathbf{a}_{\text{cor}} = 2\boldsymbol{\Omega} \times \frac{\partial \mathbf{u}_r}{\partial t}$ and $\mathbf{a}_{\text{cen}} = \boldsymbol{\Omega} \times (\boldsymbol{\Omega} \times \mathbf{r}_p)$ are the Coriolis and centrifugal acceleration induced by rotation, respectively. $\boldsymbol{\Omega}$ is the angular velocity and \mathbf{r}_p is the coordinate vector in the rotating frame. In this paper, the z axis through the center of the hollow pillar is set as the axis of rotation.

Figure 2 shows the band structures and the localized WGMs under rotation boundary conditions or not. The band structures along the direction ΓX of the irreducible Brillouin zone are plotted in Fig. 2(a), where the blue dotted lines and red dotted lines represent the dispersion curves under rotation conditions and not respectively. A pair of flat dispersion curves of the localized WGMs lie in the local resonance band gap covered by grey area from 0.185 to 0.201. It can be seen that rotation have few influences on the dispersion curves and band structures except the WGMs. When no rotation, there is only a slight frequency difference between WGMs due to the asymmetry between the directions of ΓX and ΓM . While

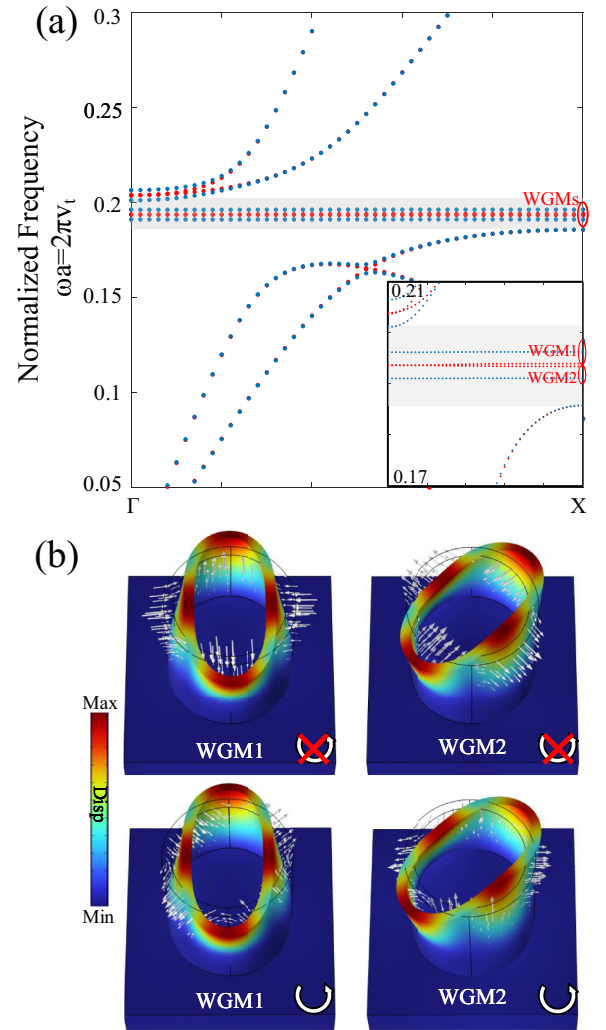


FIG. 2. Simulation results of hollow-pillar unit cells. (a) Band structures of unit cells: red dots and blue dots denote the no-rotation case and the rotation-applied case, respectively. (b) The displacement fields and deformations of WGMs under rotation or not at point X . The white arrows are the velocity vectors indicating the deformation trend.

under rotation, the dispersion curves of WGM1 and WGM2 shift equally but oppositely [39], shown in the inset. And the curves keep flat, which means these two modes remain nondispersive and localized.

Figure 2(b) shows the displacement fields and the deformations of WGMs under rotation or not at point X . The white arrows around hollow pillars are the velocity vectors of different parts, indicating the deformation trend. When no rotation conditions applied, the WGM1 and WGM2 vibrate back and forth along the directions of ΓX and ΓM , respectively. When under rotation, each part of hollow pillars is subjected to a Coriolis force [40] in the inertial coordinate system, causing the direction change of velocity vectors. It is worth noting that the changed velocity vectors make WGM1 and WGM2 tend to couple and transform each other. Therefore the displacement fields of WGMs are no longer along the specific directions but have tendency to deflect.

The displacement fields of WGMs under rotation can be regarded as the result of superposition of WGM1 and WGM2 due to (1) the coupling between these two modes caused by Coriolis force; (2) the location in bandgap, which means no disturbances by other modes. Since the features of nondispersion and localization, the WGMs can be modeled in a single unit cell. Considering the WGMs as a second-order “spring-mass-damping” system, the kinetic equation of the WGMs coupled by the Coriolis force when rotating only about the z axis can be expressed as Eq. (3) [41]:

$$\begin{aligned} M_{\text{eff}}\ddot{q} + D\dot{q} + 2m_{\text{cori}}\dot{q} \begin{pmatrix} 0 & -\Omega_z \\ \Omega_z & 0 \end{pmatrix} \\ - m_{\text{cent}}q \begin{pmatrix} \Omega_z^2 & 0 \\ 0 & \Omega_z^2 \end{pmatrix} + kq = F, \end{aligned} \quad (3)$$

where M_{eff} , q , D , K , and F are the effective mass matrix, the displacement matrix in the direction of vibration spindles, the damping matrix, the stiffness matrix, and the external force matrix of the two modes, respectively. Ω_z is the angular velocity around the z axis, and m_{cori} , m_{cent} are the Coriolis and centrifugal masses, respectively.

Given the ideal conditions of zero frequency difference, zero damping and small angular velocity, the analytical solution of Eq. (3) can be obtained by using the slow-variable averaging method [42]. The angle between the time-varying vibration spindle of WGMs and the initial spindle can be expressed Eq. (4).

$$\theta = \frac{1}{2} \arctan(q_2/q_1) \approx m_{\text{cori}} \int \Omega_z dt / (2m_{\text{eff}}). \quad (4)$$

It is illustrated that under the effect of the Coriolis force, there is precession of the WGMs in the inertial coordinate system and the precession angle is proportional to the angular velocity integral around the z axis. The theoretical precession factor (PF) is $m_{\text{cori}}/2m_{\text{eff}}$, where m_{eff} and m_{cori} can be calculated by the normalized vibration parameters of WGMs [43], so that PF can be expressed as Eq. (5):

$$FP = \frac{\int (\phi_{x1}\phi_{y2} - \phi_{y1}\phi_{x2})dV}{2(\phi_x^2 + \phi_y^2 + \phi_z^2)dV}, \quad (5)$$

where $\phi_{x,y,z}$ are the normalized displacement of WGMs along the three directions of Cartesian coordinates. And these normalized parameters can be obtained by FEM when the structure of PnC is determined. It is worth mentioning that the location of rotation axis barely affects the results because of the Coriolis force independent of the location of rotation axis and the negligible centrifugal force.

III. POINT-DEFECT PNC UNDER ROTATION

A. Structure of the point-defect PnC

Although different kinds of PnCs can be composed of hollow-pillar units and solid-pillar units in certain ways, coupled resonance will occur among more than one neighboring hollow-pillar units [44,45], complicating the interaction of the WGMs with the rotation. A point-defect PnC, shown in Fig. 3, can not only avoid coupled resonance but also strongly confine energy inside a single pillar.

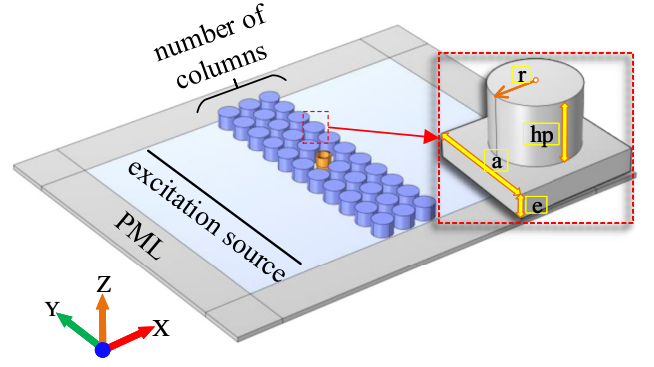


FIG. 3. Structure of the point-defect PnC. The hollow-pillar unit is the same to the unit cell in Sec. II, $hp = 0.6a$, $r = 0.45a$, and the number of columns is three. The perfect match layers (PML) are around the PnC.

In the case where the point defect (the hollow pillar) has been determined, the parameters design of this PnC should be considered for two more aspects. Firstly, the WGMs need to be in the bandgap of the complete PnC, thus eliminating the coupling and interference of other unexpected modes. Secondly, the transmission of the PnC needs to be as high as possible to obtain a stronger transmissive signal. After comprehensive consideration, the solid-pillar height is $hp = 0.6a$ and radius is $r = 0.45a$. And the band structure of the solid-pillar matrix is shown as Fig. 4(a), where the low frequency bandgap ranges from 0.175 to 0.243 and can cover the WGMs. The WGMs as the defect modes of the point-defect PnC are shown in Fig. 4(b), and it can be seen that the point defect well confines the energy and owns the displacement far larger than surroundings. The transmission spectra of the PnC with various numbers of columns are shown as Fig. 4(c). The transmission is calculated by comparing the average displacements over several wavelengths behind the PnC to the results of reference simulations with a blank substrate [36]. The three-column PnC maximizes the transmission in defect modes, but weakens the ability of the bandgap to confine the elastic waves. Notably, this trade-off is worthwhile, since the leakage waves could be eliminating by difference in Sec. III C. Another noteworthy thing is that only one resonance peak appears in the transmission spectrum. This is due to the deaf-band effect [46], and only WGM1 is excited by the Lamb waves propagating along X axis. When the lattice period a is taken as 10 mm, the parameters and properties of the point-defect PnC with hollow pillar are summarized in Table I.

B. Precession of WGMs

The point-defect PnC operated in defect modes are simulated under rotational boundary conditions, using the FEM in the time domain. The WGMs are excited continuously by Lamb waves from the excitation source, and no rotation is applied for the first 200 periods (1.66 ms) to ensure the vibration reaches steady initial state. Then a step angular velocity rotating around the z axis with a ten-period transition zone and an amplitude of Ω_z is applied to the PnC. The Ω_z greatly affects the complexity of simulation, since precise results of time-domain simulation require a calculation interval of less

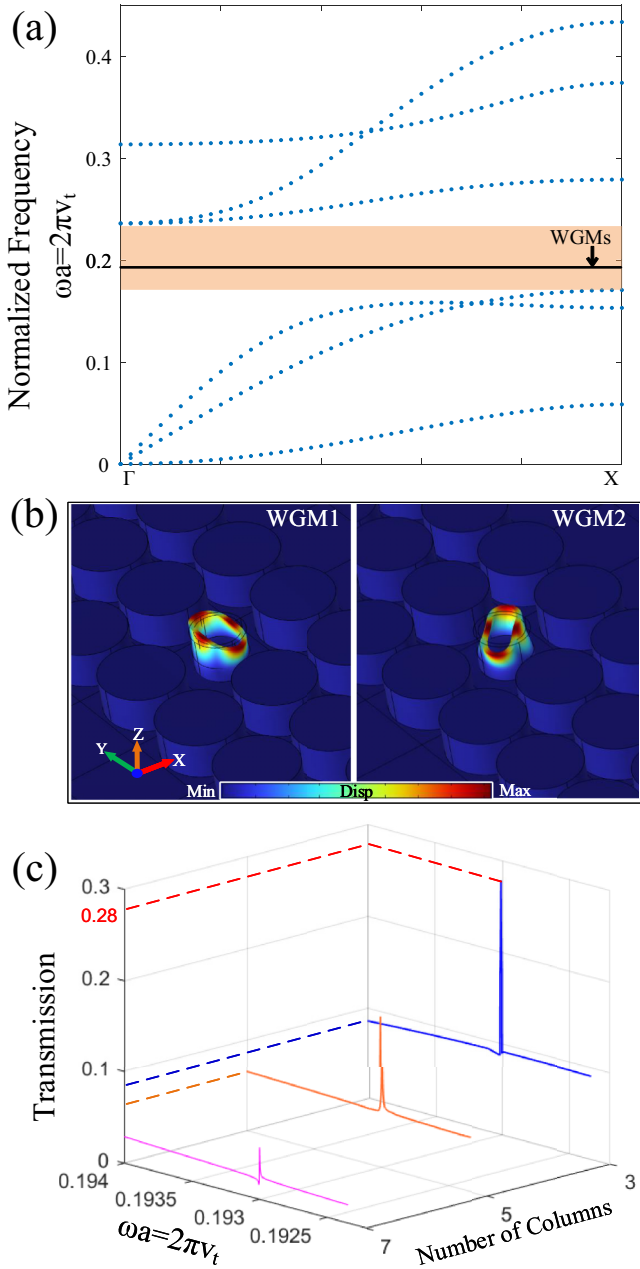


FIG. 4. Basic properties of the point-defect PnC. (a) Band structure of the solid-pillar matrix, the band gap covers WGMs of the point defect. (b) Displacement fields and deformations of WGMs in the point-defect PnC. (c) Transmission spectra of the point-defect PnC.

than one 60th of a period and the Ω_z determines how many periods need to calculate. Therefore the Ω_z is set as 0.005ω , which is able to balance the computational accuracy and complexity of FEM in the time domain of the 3D model.

The step angular velocity is obtained by customizing a step function under the top-level Global Definitions node. And the step function is a time-varying function, sharply transiting from 0 to the amplitude (0.005ω) at a certain time ($400\pi/\omega$). Subsequently, the rotation conditions are implemented under the rotating frame node by calling customized function, choosing rotation direction and locating rotation axis. The

TABLE I. Structural and characteristic parameters of the designed PnC.

Parameters and Properties	Value
material	silicon
lattice constant (a)	10 mm
thickness of plate (e)	$0.2a$
in/outside height of hollow pillar (h_i/h_o)	$0.4a/0.64a$
in/outside radius of hollow pillar ($r_o/r_o - b$)	$0.3a/0.25a$
height of solid pillar (h_p)	$0.6a$
radius of solid pillar (r)	$0.45a$
the number of columns	3
low-frequency band gap	102–142 kHz
resonant frequencies of WGMs	120.393/120.378 kHz
transmission	0.28
quality factors of WGMs	8226/7614

vibration patterns of the PnC at different moments under counterclockwise (CCW) rotation are shown in Fig. 5. Two color maps are used to display the displacement of the hollow pillar and the other parts in the PnC, respectively, because the displacement of the hollow pillar is much larger than the other parts.

The initial vibration pattern of the PnC is shown at 1.65 ms in Fig. 5. And it is worth highlighting the distinctions of the initial patterns between a point-defect PnC and a single hollow pillar on a substrate. The WGMs can still be excited even if only a single hollow pillar on a substrate, since the WGMs are the local resonance modes of a hollow pillar. However, the WGMs of the single pillar are often disturbed by other modes and have an uncertain initial vibration spindle. Benefit from the high- Q defect state of the point-defect PnC, unexpected modes can be eliminated by the band gap and energy can be confined in the defect cavity better. More importantly, due to the deaf-band effect of PnCs, the initial vibration spindle must be consistent with WGM1, which is symmetric about the wave vector of the lamb wave. After 200 periods, a CCW step angular velocity rotating around the z axis is applied to the PnC. The vibration pattern of the hollow pillar at

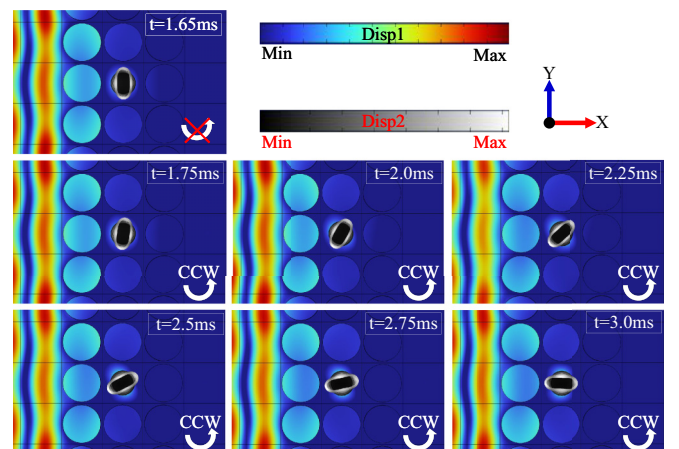


FIG. 5. The vibration pattern of PnC operated in WGMs at different moments under CCW rotation.

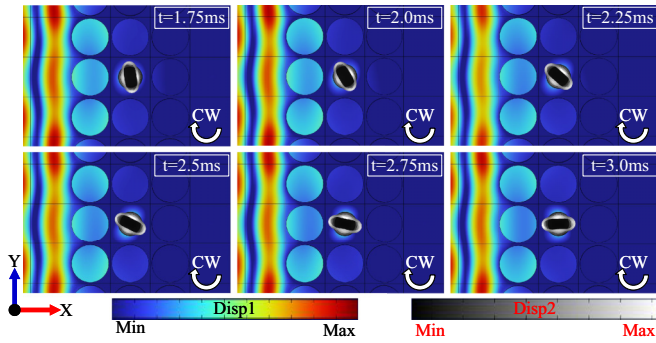


FIG. 6. The vibration pattern of PnC operated in WGMs at different moments under CW rotation.

equal intervals between 1.75 and 3.0 ms indicates that the vibration pattern undergoes clockwise (CW) precession under the CCW angular velocity. In other words, the vibration pattern lags behind the rotation of the PnC. The precession angle reaches 45° at about 2.25 ms, indicating the energy of WGM1 is completely coupled into WGM2. And the WGM2, which should be suppressed by the deaf-band effect, is completely excited. However, this state is temporary, and the precession will continue under continuous rotation. At almost 3.0 ms, the vibration pattern has undergone 90° precession and reverts to WGM1, thus the above process will be repeated periodically.

Figure 6 shows the vibration pattern of the hollow pillar at equal intervals between 1.75 and 3.0 ms under the CW rotation. It can be seen that the vibration pattern owns the opposite-direction precession but the same absolute precession angle compared to the case under CCW rotation. This is because the change in the direction of rotation reverses the direction of the Coriolis force but does not affect its magnitude. Therefore the vibration pattern of the hollow pillar in the PnC is directional depending on the direction of rotation.

In order to describe the precession of WGMs in the inertial space intuitively, the Lissajous figures (the horizontal axis is the displacement along the vibration spindle of WGM1 and the vertical axis is of WGM2) are plotted in Fig. 7. Half of the precession period (WGM1 to WGM2) rather than the whole precession period (WGM1 to WGM2 and back to WGM1) is plotted in the Lissajous figure for a clearer presentation.

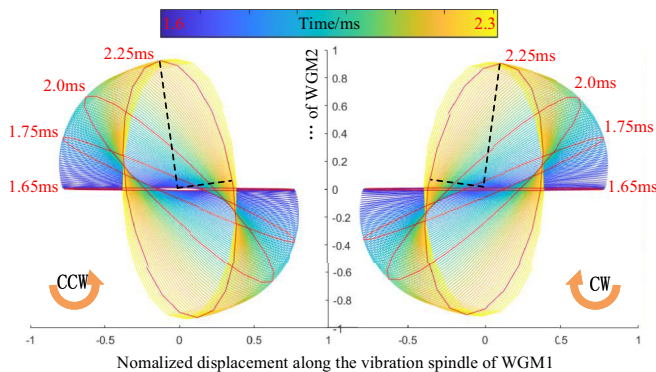


FIG. 7. Lissajous figures of WGMs for half a precession period. The red ellipses marked by times correspond to the vibration patterns at the corresponding moments in Figs. 5 and 6.

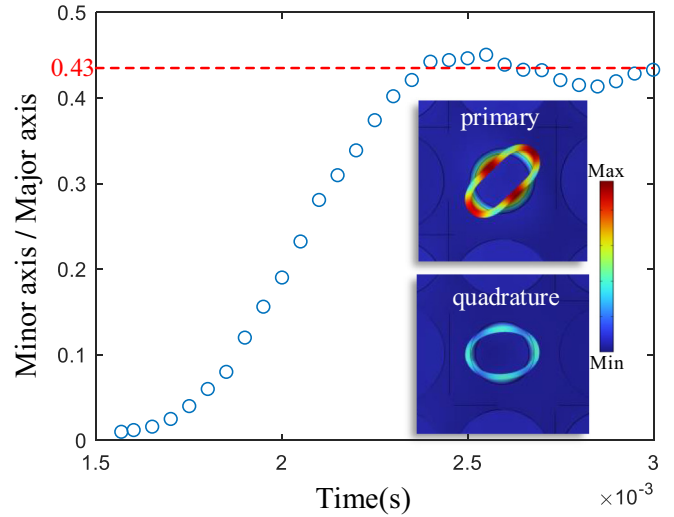


FIG. 8. Trend of the minor axis of the elliptical trajectories with time in the Lissajous figure. The inset exemplifies the primary and the quadrature modes when the vibration pattern is processed by 45° .

The process that the major axis of elliptical trajectory rotates from the transverse axis to the longitudinal axis indicates the precession of the vibration pattern from WGM1 to WGM2. The trajectories marked by various times in Fig. 7 correspond to the vibration patterns in Figs. 5 and 6, respectively. Therefore the WGMs in the hollow pillar have a directional and continuous precession phenomenon under rotation.

It is worth noting that the minor axis of the elliptical trajectory in Lissajous figure lengthens gradually. The minor axis represents the amplitude of the quadrature mode relative to the primary mode, and the quadrature mode differs from the primary mode by 90° phase in time and by 45° angle between the vibration spindles in space. Figure 8 specifies the trend that the minor axis become longer and longer and finally tend to stabilize. It indicates that the energy of the primary vibration mode gradually is coupled to the quadrature mode during the precession process and into a stable state finally, where the ratio of the amplitude of the quadrature mode to the primary mode is 0.43. The larger the ratio between the quadrature mode and the primary mode, the lower the resolution of the precession. And when the ratio is 1, the ability of precession will be completely lost. However, this quadrature mode is difficult to be eliminated in the open-loop simulation of this paper, and needs to be suppressed by additional feedback.

To specify the numerical relationship between the precession and the angular velocity, we plot the variation of the precession angle with time before and after the step angular velocity is applied, as shown in Fig. 9, taking the case under CW rotation as an example. The red-circle marks in the figure represent the precession angle relative to the inertial space at that moment, and the precession angle varies with time when the angular velocity is applied. A linear fit with a R^2 of 0.998 is obtained, showing that the precession angle has a good linear relationship with time or with the integral of the step angular velocity in time. The theoretical results for the determined PnC are calculated according to Eq. (5) and summarized in Table II. Compared with theoretical results

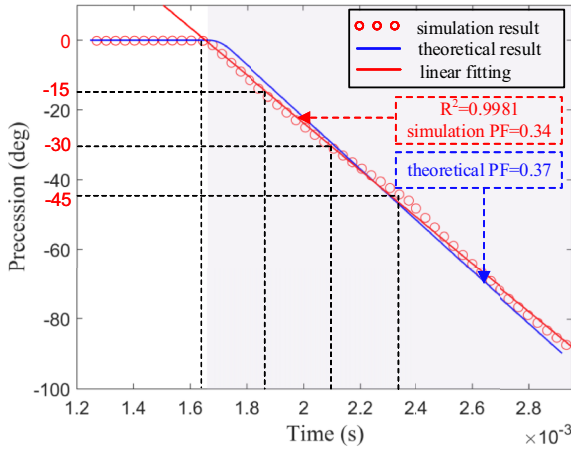


FIG. 9. Trend of precession angle with time under step angular velocity. The red circles represent the simulation results and are fitted by the red solid line. The blue solid line represent the theoretical results, and the purple zone indicates the rotation condition is applied.

(blue solid line), the PF of a time-domain simulation results 0.34 is slightly different from the theoretical PF of 0.37. This is because the derivation of the theoretical results is based on the ideal condition of no frequency difference, no damping and isotropy, while the simulation can only make the simulation condition converge to but not reach the ideal condition. However, it can still be found that time-domain simulation results agree with the theoretical results well. It not only illustrates the linear relationship between the precession and the integral of angular velocity but also verifies the rationality and correctness of the simulation from the side.

C. Transmissive waves under rotation

The transmissive waves of the point-defect PnC are also affected by rotation. This is because that the hollow pillar operated in WGMs functions as a coupled-resonant waveguide by evanescent waves [21,47], and the changes of WGMs can modulate the output. It is evident in Sec. II B that WGMs will undergo precession in the time domain under rotation. Therefore the transmissive waves are affected accordingly.

Figure 10 shows the displacement fields of transmissive elastic waves in the substrate plate at different precession angles, and the simulation conditions are the same to the descriptions in Sec. II B. The cases of 0° , 15° , 30° , and 45° precession are captured, respectively, and they correspond to the points marked in Fig. 9. Only the displacement fields behind PnC are captured due to the large differences compared to the displacement fields in front of PnC. In the initial no-precession state, the transmissive elastic waves are symmetrical with respect to the midline and the elastic waves at

TABLE II. Effective mass, Coriolis mass and theoretical PF of WGMs in the point-defect PnC.

m_{eff} (kg)	m_{cori} (kg)	Theoretical PF
1.75×10^{-5}	1.31×10^{-5}	0.37

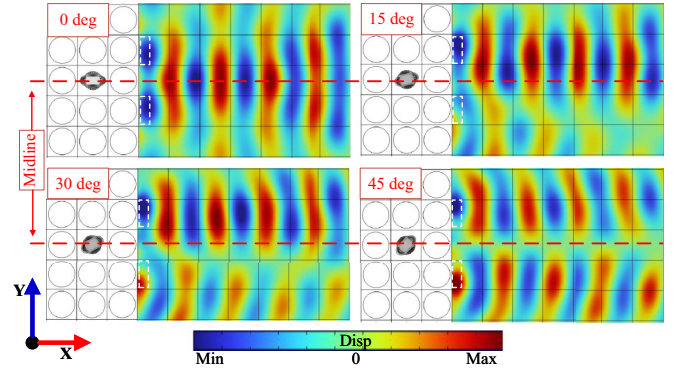


FIG. 10. Distribution of the transmissive elastic waves in the substrate plate under different precession angles. The red line is the midline of the PnC, and the white dashed areas are the sampling area of phase.

the upper and lower parts of the midline are in phase. This is owing to the symmetry of WGM1 with respect to the propagation direction of the Lamb waves and the midline of the PnC. However, the symmetry will be broken when the precession occurs, and the transmissive waves at the upper and lower parts are also no longer in phase. Shown as the cases in Fig. 10, the displacement at the white box in the lower half of the midline gradually turns from negative to positive with the precession angle increasing. Eventually, when at 45° precession, WGM2 becomes the dominant mode of the PnC, and the transmissive waves at the upper and lower parts are antiphase due to the antisymmetry of WGM2. In fact, considering the two-antinode symmetry of WGMs, when the precession angle exceeds 45° , the displacement fields of the transmissive waves will be the same as its complementary angle.

The relationship of the phase difference between the transmissive waves in the upper and lower parts with the precession angles is plotted as Fig. 11. The phase difference is obtained by the inverse cosine of the ratio of the displacement in lower

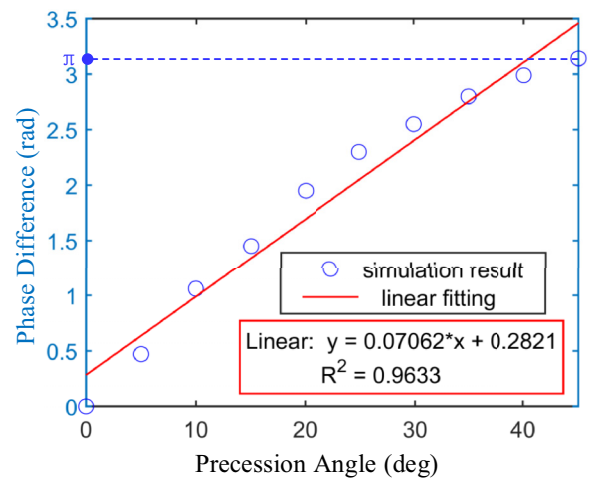


FIG. 11. Relationship between the precession angle and the phase difference of the displacements in the two white dashed areas symmetrical about the midline of the PnC. A linear fit of 0.96 is obtained and the phase gain K is fixed (0.07 rad/deg or 4 rad/rad).

box to its amplitude when the displacement in upper box reaches its maximum. A linear fit with a R^2 of 0.96 is obtained, showing a good linear relationship within a 45° precession range. Since the initial state of no precession always results in zero phase difference and the 45° precession always results in antiphase, the phase gain K (0.07 rad/deg or 4 rad/rad) between the precession angle and phase difference in this linear relationship is relatively fixed and is not related to the structure neither the angular velocity. In fact, the effects of rotation on the transmissive waves can be better characterized by the difference displacement between the upper and lower parts due to (1) a continuous variable easier to detect than phase and (2) a way to eliminate the leakage waves not affected by the precession. Since the frequency of phase change is much lower than that of transmissive waves, the phase change can be treated as a slow variable which keeps constant within a period of the transmissive waves. And the difference displacement is deduced (see Appendix) as

$$\begin{aligned} \Delta D_{\text{extre}} &= -2CTD_0 \sin(\Delta\varphi/2) \\ &= -2CTD_0 \sin\left(K \cdot PF \cdot \int_0^t \Omega_z(\tau) d\tau/2\right) \\ &\approx \underbrace{-C \cdot T \cdot K \cdot PF \cdot D_0}_{\text{scalefactor}} \int_0^t \Omega_z(\tau) d\tau \Big|_{\Delta\varphi \rightarrow 2k\pi}, \quad (6) \end{aligned}$$

where D_{extre} is the extremums of the difference displacement, C is the proportional constant, T is the transmission of the PnC, D_0 is the amplitude of the incident waves, and $\Delta\varphi$ is the phase change, which will set to zero periodically when it exceeds 2π . For a determined PnC and incident wave, C , T , K , PF , and D_0 are all fixed. Therefore D_{extre} is only related to the integral of the angular velocity.

Equation (6) predicts three characteristics of transmissive waves under rotation, namely periodicity, linearity and directionality. Specifically, periodicity is indicated by the half-sine function of D_{extre} ; Linearity is approximated when at small precession angles, and the scale factor is expressed as $SF = -C \cdot T \cdot K \cdot PF$; directionality is reflected by the odd function of D_{extre} .

To verify the predictions, Fig. 12 displays the simulation results of the effects of rotation on the difference displacement. Notably, the boundary conditions are applied as described in Sec. III B. The inset in Fig. 12(a) covers the whole process from the static state to the state undergoing 180° precession (a full circle in the Lissajous figure), while the main figure intercepts the process in the red zone. Clearly, the difference displacement keeps extremely small during the first 200 periods (1.66 ms), even if there exist leakage waves and disturbance from the unstable initial vibration. Additionally, the extremums of difference displacement vary gradually with time in a tendency of half-sine function after 200 periods, which indicates the periodicity. The peaks and valleys result from the out-phase and in-phase transmissive waves, corresponding to the moments when the precession of WGMs at $(2k+1)\pi/4$ and $k\pi/2$ ($k=0, 1, 2, \dots$), respectively.

Specifically, during the process covered by red zone, the extremums of difference displacement have a linear

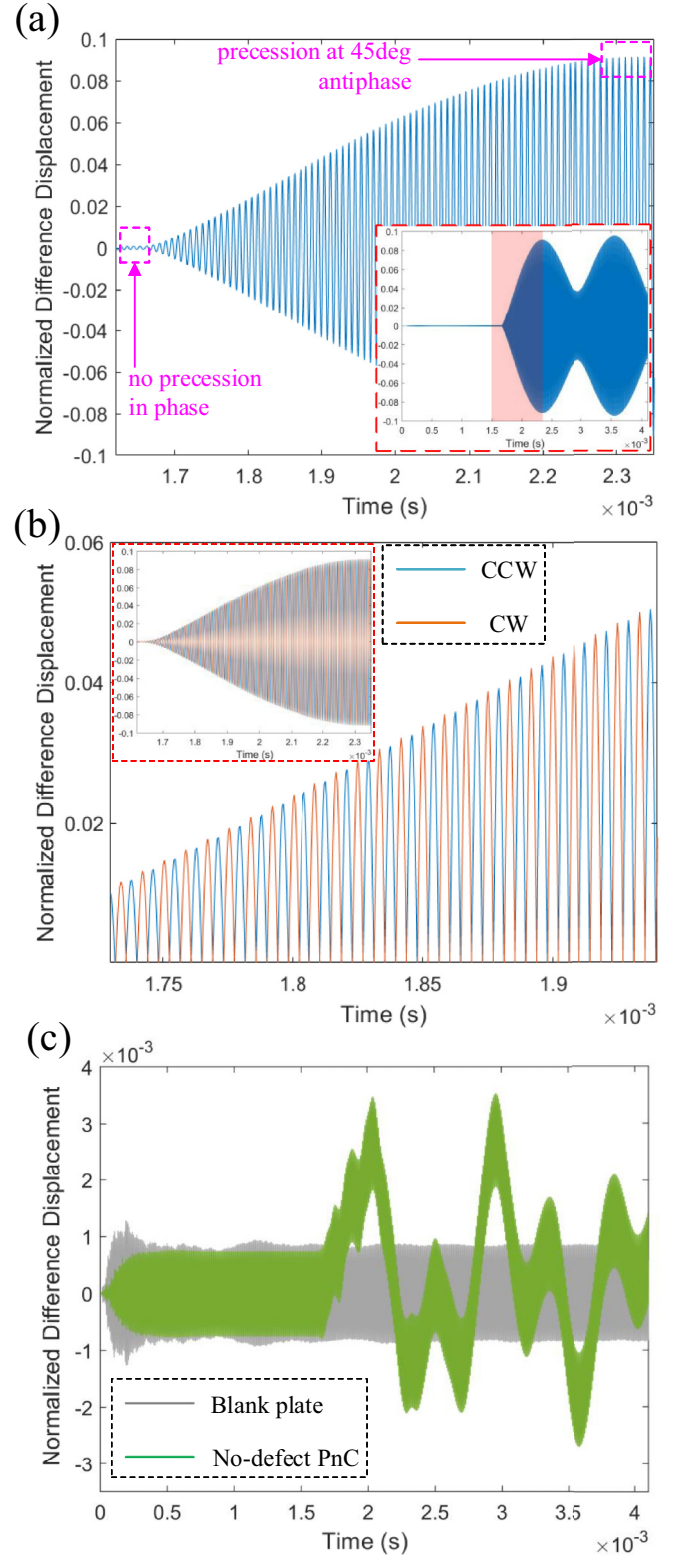


FIG. 12. Trend of difference displacement with time. The inset in (a) shows the difference displacement during the whole precession process, indicating the periodicity. The main figure of (a) enlarges the red zone of the inset, reflecting the linearity. (b) compares the difference displacement under CW and CCW rotations, revealing the directionality. (c) shows the results of two reference cases.

relationship with time or the precession visibly at small precession angles, reflecting the linearity. Nevertheless, it is worth mentioning that the extremums of difference displacement should have return to zero after a period rather than floating with a certain error. It is caused by the quadrature mode mentioned in Sec. III B and need to be suppressed by further feedback. Compared with two reference cases of a blank plate and a no-defect PnC under the same boundary conditions, the reference results shown in Fig. 12(c) are remarkably tiny. Therefore The periodic changes in transmissive waves are exclusively caused by the precession of WGMs. Figure 12(b) compares the results between the two cases of CW and CCW rotation around the z axis. The inset considers the process from the imminent start of precession to precession through 45° , while the main figure intercepts and enlarges the red-zone part of the inset. Obviously, the difference displacement under different-direction rotation has similar variation trends. However, they keep steadily different from each other by 180° phase, or keep opposite in other words, revealing the directionality. Therefore the simulation results are in high agreement with the predictions of Eq. (6), which illustrates the rationality and correctness of the simulation.

IV. DISCUSSION

In this paper, we study the roles of rotation on the WGMs in PnCs, especially in the point-defect PnC. And the simulation results demonstrate that transmissive waves are modulated by rotation or precession, which feature periodicity, linearity and directionality. Further, these features can be utilized to measure the integral of angular velocity as an all-solid-state gyroscope scheme. In detail, by counting the periodic envelopes, the number of times WGM1 and WGM2 are transformed into each other can be known, and each transformation means 45° precession. By the magnitude of D_{extre} , the precession angle during a period can be obtained according to the linear relation. By the phase change of the waveform, the direction of rotation can be judged based on the directionality. Combining the three, the total precession angle can be deduced. Since the total precession angle is linearly proportional to the integral of angular velocity applied to the PnC, the actual rotation angle of the PnC can be obtained. In practical experiments, the time-domain signals of transmissive waves at the symmetrical parts can be detected by the symmetrically distributed piezoelectric lead zirconate titanate (PZTs), which are widely applied to detect Lamb waves [48,49]. Subsequently, the two analog electrical signals of symmetrical parts are input to a lock-in amplifier (LIA) to be demodulated (phase-sensitive demodulation). The excitation signal of Lamb waves is chosen as the reference signal. As a result, both the amplitude and phase of the difference signal relative to the reference signal are obtained.

Unlike the existing all-solid-state gyroscopes using the SAW waves in substrate to sense rotation [50–52], the above scheme detects rotation by the high- Q WGMs, thus potential for higher sensitivity. Moreover, this scheme is rate-integrating, therefore the bandwidth depends on the low-pass filter of demodulator and is wider than the bandwidth of rate scheme ($\propto \omega/Q_{\text{sense}}$). Most importantly, the limitation

of weak output in typical SAW gyroscopes [33,53–55] is expected to be overcome in this scheme. It benefits from dependency of the amplitude of D_{extre} on the transmission T of PnC. In this paper, a normalized amplitude of about 0.1 is obtained eventually, and it can be further improved by optimized the transmission of the PnC.

V. CONCLUSION

The effects of rotation on a PnC operated in WGMs are numerically investigated for the first time with FEM. All structures have been carefully designed and constructed in COMSOL. The band structures of the hollow-pillar units indicate that rotation has few influences on the other dispersion curves except WGMs, and the WGMs have tendency to deflect. Specifically for a point-defect PnC, the theoretical analyses and FEM results show that the vibration pattern of the WGMs under the action of rotation will undergo a precession. And the precession angle is proportional to the integral of angular velocity with a precession factor of 0.34, which is very close to the theoretical value. In addition, the phase difference between the transmissive waves in the upper and lower parts is nearly linearly related to the precession angle. And the zero precession always results in zero phase difference while the 45° precession always results in antiphase. Furthermore, the difference displacement between the transmissive waves is utilized to eliminate the leakage waves and characterize the effects of rotation better. The difference displacement offers a rate-integrating scheme to sense rotation due to its periodicity, linearity and directionality. Compared with the existing SAW gyroscopes, this rotation-sensing scheme features potential for higher sensitivity, wider bandwidth and strong output. We believe that these findings have promising applications especially in high-performance SAW gyroscopes.

ACKNOWLEDGMENTS

The authors would like to acknowledge the financial support from the National Natural Science Foundation of China (Grant No. 62071118) and the Primary Research and Development Plan of Jiangsu Province (BE2021004-3).

APPENDIX: DERIVATION OF THE DIFFERENCE DISPLACEMENT

Ideally, the phase difference of the transmissive waves between the upper and lower areas due to the rotation can be expressed as

$$\Delta\varphi(t) = K \cdot PF \cdot \int_0^t \Omega_z(\tau) d\tau, \quad (\text{A1})$$

where K and PF are fixed under the determined structure. Due to the symmetry of the vibration pattern, $\Delta\varphi$ will set to zero periodically when it exceeds 2π . In fact, the transmissive waves often include leakage waves, which are not affected by the precession. To eliminate the interference from leakage waves, the difference displacement between the upper and lower areas is utilized to characterize the phase difference. Assuming that the transmissive waves are cosine waves with the same frequency as the WGMs, the difference displacement

between the two areas can be expressed as

$$\begin{aligned} \Delta D &= D_{\text{upper}} - D_{\text{lower}} = T \cdot D_0 [\cos(\omega t + \Delta\varphi) - \cos(\omega t)] \\ &= T \cdot D_0 \left[\underbrace{\cos(\omega t)}_{\text{slow variable}} (\underbrace{\cos \Delta\varphi - 1}_{\text{slow variable}}) - \underbrace{\sin(\omega t)}_{\text{slow variable}} (\underbrace{\sin \Delta\varphi - 1}_{\text{slow variable}}) \right], \end{aligned} \quad (\text{A2})$$

where T and D_0 are the transmission of the PnC and the amplitude of the incident waves, respectively. Since $\Delta\varphi$ in Eq. (A2) is also a time-dependent variable, it is difficult to directly represent the relationship between the phase difference and the difference displacement. Since the frequency of the applied angular velocity is much lower than the frequency of the WGMs, the change rate of the phase difference will also be much slower than the transmissive waves. Therefore the terms containing $\Delta\varphi$ can be regarded as slow variables which keep constant within one vibration period of the transmissive waves, and Δ becomes a superposition of two quadrature terms of the fast variables. It can be seen that in the long term the trajectory of Δ with time will be a fast oscillation,

while the peak of the oscillation varies slowly with $\Delta\varphi$. Δ has two extremums in each vibration period, obtained at $\dot{\Delta} = 0$, and the phase of the fast variables needs to satisfy $\tan \omega t = \cot(\Delta\varphi/2)$. Thus a set of particular solutions of the two quadrature terms can be expressed as

$$\begin{aligned} \sin \omega t &= C \cos(\Delta\varphi/2), \\ \cos \omega t &= C \sin(\Delta\varphi/2), \end{aligned} \quad (\text{A3})$$

where C is the proportional constant. An expression for the relationship between the extremums of the ΔD and $\Delta\varphi$ or angular velocity Ω_z can be obtained by substituting Eq. (A3) back into Eq. (A2):

$$\begin{aligned} \Delta D_{\text{extre}} &= -2CTD_0 \sin(\Delta\varphi/2) \\ &= -2CTD_0 \sin \left(K \cdot PF \cdot \int_0^t \Omega_z(\tau) d\tau / 2 \right) \\ &\approx \underbrace{-C \cdot T \cdot K \cdot PF}_{\text{scale factor}} \cdot D_0 \int_0^t \Omega_z(\tau) d\tau |_{\Delta\varphi \rightarrow 2k\pi}. \end{aligned} \quad (\text{A4})$$

-
- [1] Z. Alrowaili, M. Aouassa, M. Mahmoud, K. S. El-Nasser, H. A. Elsayed, T. Taha, A. M. Ahmed, A. Hajjiah, and A. Mehaney, Locally resonant porous phononic crystal sensor for heavy metals detection: A new approach of highly sensitive liquid sensors, *J. Mol. Liq.* **369**, 120964 (2023).
- [2] R. Sharaf, S. Darbari, and A. Khelif, Vertical surface phononic Mach-Zehnder interferometer, *Phys. Rev. Appl.* **19**, 024071 (2023).
- [3] S. E. Zaki, M. A. Basyooni, W. Belaid, M. Tihit, J. E. F. Ibrahim, and G. Attia, Terahertz resonance frequency through ethylene glycol phononic multichannel sensing via 2D MoS₂/PtSe₂ structure, *Mater. Chem. Phys.* **292**, 126863 (2022).
- [4] A. Biçer, A. S. Durmuslar, N. Korozlu, and A. Cicek, An acoustic add-drop filter in a phononic crystal for high-sensitivity detection of methanol in ethanol in the liquid phase, *IEEE Sens. J.* **22**, 14799 (2022).
- [5] F. Gao, S. Benchabane, A. Bermak, S. Dong, and A. Khelif, On-chip tightly confined guiding and splitting of surface acoustic waves using line defects in phononic crystals, *Adv. Funct. Mater.* **33**, 2213625 (2023).
- [6] Y. Zhou, N. Zhang, D. J. Bisharat, R. J. Davis, Z. Zhang, J. Friend, P. R. Bandaru, and D. F. Sievenpiper, On-chip unidirectional waveguiding for surface acoustic waves along a defect line in a triangular lattice, *Phys. Rev. Appl.* **19**, 024053 (2023).
- [7] D. Hatanaka and H. Yamaguchi, Real-space characterization of cavity-coupled waveguide systems in hypersonic phononic crystals, *Phys. Rev. Appl.* **13**, 024005 (2020).
- [8] H.-W. Dong, Y.-S. Wang, and C. Zhang, Inverse design of high- Q wave filters in two-dimensional phononic crystals by topology optimization, *Ultrasonics* **76**, 109 (2017).
- [9] X. Zhang, Y. Li, Y. Wang, Z. Jia, and Y. Luo, Narrow-band filter design of phononic crystals with periodic point defects via topology optimization, *Int. J. Mech. Sci.* **212**, 106829 (2021).
- [10] J. Dhillon, E. Walker, A. Krokhnin, and A. Neogi, Energy trapping in a phononic crystal cavity enhanced by nonreciprocal acoustic wave transmission, *Appl. Acoust.* **203**, 109192 (2023).
- [11] Z. He, G. Zhang, X. Chen, Y. Cong, S. Gu, and J. Hong, Elastic wave harvesting in piezoelectric-defect-introduced phononic crystal microplates, *Int. J. Mech. Sci.* **239**, 107892 (2023).
- [12] Y. M. Luo, T. T. Huang, Y. Zhang, H. H. Xu, Y. M. Xie, and X. Ren, Novel meter-scale seismic metamaterial with low-frequency wide bandgap for Lamb waves, *Eng. Struct.* **275**, 115321 (2023).
- [13] X. An, X. Yuan, and H. Fan, Meta-kagome lattice structures for broadband vibration isolation, *Eng. Struct.* **277**, 115403 (2023).
- [14] L. Mercadé, R. Ortiz, A. Grau, A. Griol, D. Navarro-Urrios, and A. Martínez, Engineering multiple GHz mechanical modes in optomechanical crystal cavities, *Phys. Rev. Appl.* **19**, 014043 (2023).
- [15] G. Madiot, R. C. Ng, G. Arregui, O. Florez, M. Albrechtsen, S. Stobbe, P. D. García, and C. M. Sotomayor-Torres, Optomechanical generation of coherent GHz vibrations in a phononic waveguide, *Phys. Rev. Lett.* **130**, 106903 (2023).
- [16] T.-T. Wu, Z.-G. Huang, and S. Lin, Surface and bulk acoustic waves in two-dimensional phononic crystal consisting of materials with general anisotropy, *Phys. Rev. B* **69**, 094301 (2004).
- [17] J.-H. Sun and T.-T. Wu, Propagation of surface acoustic waves through sharply bent two-dimensional phononic crystal waveguides using a finite-difference time-domain method, *Phys. Rev. B* **74**, 174305 (2006).
- [18] S. Benchabane, O. Gaiffe, R. Salut, G. Ulliac, V. Laude, and K. Kokkonen, Guidance of surface waves in a micron-scale phononic crystal line-defect waveguide, *Appl. Phys. Lett.* **106**, 081903 (2015).
- [19] A. Khelif, B. Aoubiza, S. Mohammadi, A. Adibi, and V. Laude, Complete band gaps in two-dimensional phononic crystal slabs, *Phys. Rev. E* **74**, 046610 (2006).

- [20] J.-C. Hsu and T.-T. Wu, Efficient formulation for band-structure calculations of two-dimensional phononic-crystal plates, *Phys. Rev. B* **74**, 144303 (2006).
- [21] Y.-F. Wang, T.-T. Wang, J.-P. Liu, Y.-S. Wang, and V. Laude, Guiding and splitting lamb waves in coupled-resonator elastic waveguides, *Comp. Struct.* **206**, 588 (2018).
- [22] N. Kherraz, F.-H. Chikh-Bled, R. Sainidou, B. Morvan, and P. Rembert, Tunable phononic structures using Lamb waves in a piezoceramic plate, *Phys. Rev. B* **99**, 094302 (2019).
- [23] Y. Liu, A. Talbi, B. Djafari-Rouhani, L. Drbohlavová, V. Mortet, O. B. Matar, P. Pernod *et al.*, Interaction of Love waves with coupled cavity modes in a 2D Holey phononic crystal, *Phys. Lett. A* **383**, 1502 (2019).
- [24] Y. Jin, N. Fernez, Y. Pennec, B. Bonello, R. P. Moiseyenko, S. Hémon, Y. Pan, and B. Djafari-Rouhani, Tunable waveguide and cavity in a phononic crystal plate by controlling whispering-gallery modes in hollow pillars, *Phys. Rev. B* **93**, 054109 (2016).
- [25] Y. Jin, Y. Pennec, Y. Pan, and B. Djafari-Rouhani, Phononic crystal plate with hollow pillars actively controlled by fluid filling, *Crystals* **6**, 64 (2016).
- [26] Y. Jin, Y. Pennec, Y. Pan, and B. Djafari-Rouhani, Phononic crystal plate with hollow pillars connected by thin bars, *J. Phys. D* **50**, 035301 (2017).
- [27] W. Yuan, J. Zhao, B. Bonello, B. Djafari-Rouhani, X. Zhang, Y. Pan, and Z. Zhong, Compact waveguide and guided beam pattern based on the whispering-gallery mode of a hollow pillar in a phononic crystal plate, *Phys. Rev. Appl.* **10**, 034010 (2018).
- [28] Muhammad, C. Lim, J. Reddy, E. Carrera, X. Xu, and Z. Zhou, Surface elastic waves whispering gallery modes based subwavelength tunable waveguide and cavity modes of the phononic crystals, *Mech. Adv. Mater. Struct.* **27**, 1053 (2020).
- [29] J. Sun, S. Yu, Y. Zhang, Q. Li, X. Xi, K. Lu, X. Wu, and D. Xiao, 0.79 ppm scale-factor nonlinearity whole-angle microshell gyroscope realized by real-time calibration of capacitive displacement detection, *Microsyst. Nanoeng.* **7**, 79 (2021).
- [30] Z. Xu, B. Xi, G. Yi, and C. K. Ahn, High-precision control scheme for hemispherical resonator gyroscopes with application to aerospace navigation systems, *Aerosp. Sci. Technol.* **119**, 107168 (2021).
- [31] Z. Xu, W. Zhu, G. Yi, and W. Fan, Dynamic modeling and output error analysis of an imperfect hemispherical shell resonator, *J. Sound Vib.* **498**, 115964 (2021).
- [32] H. Oh, K. J. Lee, K. Lee, and S. S. Yang, Gyroscopes based on surface acoustic waves, *Micro Nano Syst. Lett.* **3**, 1 (2015).
- [33] L. Tian, Q. Shen, and H. Chang, A novel progressive wave gyroscope based on acousto-optic effects, *Microsyst. Nanoeng.* **8**, 95 (2022).
- [34] S. Teymouri, H. Ahmadi, A. Rostami, and S. Matloub, Phononic crystal locally-resonant cavity for sensing metallic oxides nano-powders, *Int. J. Mech. Sci.* **207**, 106658 (2021).
- [35] S.-H. Jo, H. Yoon, Y. C. Shin, W. Choi, C.-S. Park, M. Kim, and B. D. Youn, Designing a phononic crystal with a defect for energy localization and harvesting: Supercell size and defect location, *Int. J. Mech. Sci.* **179**, 105670 (2020).
- [36] B. Ash, S. Worsfold, P. Vukusic, and G. Nash, A highly attenuating and frequency tailorable annular hole phononic crystal for surface acoustic waves, *Nat. Commun.* **8**, 174 (2017).
- [37] C. Pouya and G. R. Nash, Sub-and supersonic elastic waves in an annular hole phononic metamaterial, *Commun. Mater.* **2**, 55 (2021).
- [38] C. Multiphysics, Structural mechanics module users guide, 2022.
- [39] K. Li, H. Fu, and Y. Li, Coriolis-force-induced coupling between two modes of a mechanical resonator for detection of angular velocity, *Phys. Rev. A* **98**, 023862 (2018).
- [40] M. Jammer, *Concepts of Force: A Study in the Foundations of Dynamics* (Courier Corporation, 1999).
- [41] L. Meirovitch, *Analytical Methods in Vibrations* (Prentice Hall, 1967).
- [42] D. D. Lynch, Vibratory gyro analysis by the method of averaging, in *Proceedings of the 2nd St. Petersburg Conference on Gyroscopic Technology and Navigation* (Elektropribor, 1995), pp. 26–34.
- [43] J. Y. Cho, High-Performance Micromachined Vibratory Rate- and Rate-Integrating Gyroscopes., Ph.D. thesis, 2012.
- [44] S.-H. Jo, Y. C. Shin, W. Choi, H. Yoon, B. D. Youn, and M. Kim, Double defects-induced elastic wave coupling and energy localization in a phononic crystal, *Nano Convergence* **8**, 27 (2021).
- [45] H. Kähler, D. Platz, and S. Schmid, Surface acoustic wave coupling between micromechanical resonators, *Commun. Phys.* **5**, 118 (2022).
- [46] M. M. Indaleeb, S. Banerjee, H. Ahmed, M. Saadatzi, and R. Ahmed, Deaf band based engineered dirac cone in a periodic acoustic metamaterial: A numerical and experimental study, *Phys. Rev. B* **99**, 024311 (2019).
- [47] Y.-F. Wang, V. Laude, and Y.-S. Wang, Coupling of evanescent and propagating guided modes in locally resonant phononic crystals, *J. Phys. D* **47**, 475502 (2014).
- [48] B. Lin and V. Giurgiutiu, Modeling and testing of PZT and PVDF piezoelectric wafer active sensors, *Smart Mater. Struct.* **15**, 1085 (2006).
- [49] Y. Zheng, K. Liu, Z. Wu, D. Gao, R. Gorgin, S. Ma, and Z. Lei, Lamb waves and electro-mechanical impedance based damage detection using a mobile PZT transducer set, *Ultrasonics* **92**, 13 (2019).
- [50] S. W. Lee, J. W. Rhim, S. W. Park, and S. S. Yang, A micro rate gyroscope based on the saw gyroscopic effect, *J. Micromech. Microeng.* **17**, 2272 (2007).
- [51] W. Wang, H. Oh, K. Lee, S. Yoon, and S. Yang, Enhanced sensitivity of novel surface acoustic wave microelectromechanical system-interdigital transducer gyroscope, *Jpn. J. Appl. Phys.* **48**, 06FK09 (2009).
- [52] H. Oh, K. Lee, S. S. Yang, and W. Wang, Enhanced sensitivity of a surface acoustic wave gyroscope using a progressive wave, *J. Micromech. Microeng.* **21**, 075015 (2011).
- [53] V. Varadan, W. Suh, P. Xavier, K. Jose, and V. Varadan, Design and development of a MEMS-IDT gyroscope, *Smart Mater. Struct.* **9**, 898 (2000).
- [54] R. C. Woods, H. Kalami, and B. Johnson, Evaluation of a novel surface acoustic wave gyroscope, *IEEE Transactions on Ultrasonics, Ferroelectrics, and Frequency Control* **49**, 136 (2002).
- [55] M. Lee and K. Lee, Enhancing the sensitivity of three-axis detectable surface acoustic wave gyroscope by using a floating thin piezoelectric membrane, *Jpn. J. Appl. Phys.* **56**, 06GN14 (2017).